micromachines

MDPI

Article

Electric Field Induced Electrorotation of 2D Perovskite Microplates

Ruifu Zhou [1], Daobiao Hong [2], Siyu Gao [3], Yu Gu [2,*] and Xuhai Liu [1,*]

1 College of Microtechnology & Microtechnology, Qingdao University, Qingdao 266071, China; 2020020607@qdu.edu.cn
2 College of Materials Science and Engineering, Nanjing University of Science and Technology, Nanjing 210094, China; daobiaohong@mail.sim.ac.cn
3 Materials Science and Engineering Department, Carnegie Mellon University, Pittsburgh, PA 15219, USA; siyugao@andrew.cmu.edu
* Correspondence: yug@njust.edu.cn (Y.G.); xuhai@qdu.edu.cn (X.L.)

Abstract: High precision-controlled movement of microscale devices is crucial to obtain advanced miniaturized motors. In this work, we report a high-speed rotating micromotor based on two-dimensional (2D) all-inorganic perovskite $CsPbBr_3$ microplates controlled via alternating-current (AC) external electric field. Firstly, the device configuration with optimized electric field distribution has been determined via systematic physical simulation. Using this optimized biasing configuration, when an AC electric field is applied at the four-electrode system, the microplates suspended in the tetradecane solution rotate at a speed inversely proportional to AC frequency, with a maximum speed of 16.4 × 2π rad/s. Furthermore, the electrical conductivity of $CsPbBr_3$ microplates has been determined in a contactless manner, which is approximately 10^{-9}–10^{-8} S/m. Our work has extended the investigations on AC electric field-controlled micromotors from 1D to 2D scale, shedding new light on developing micromotors with new configuration.

Keywords: perovskites; nanomotor; AC voltage; contactless measurement; nanosheet

Citation: Zhou, R.; Hong, D.; Gao, S.; Gu, Y.; Liu, X. Electric Field Induced Electrorotation of 2D Perovskite Microplates. *Micromachines* **2021**, *12*, 1228. https://doi.org/10.3390/mi12101228

Academic Editors: Anurag Krishna and Hong Zhang

Received: 17 September 2021
Accepted: 5 October 2021
Published: 9 October 2021

1. Introduction

High precision-controlled movements of micro-objects are crucial for achieving advanced micro- and nanomotors [1–3], which might enable a plethora of various cutting-edge applications, such as drug delivery for in-vivo treatment [4,5], environmental remediation [6,7], biosensor and other bio-chemical implementations [8–10]. Current related research efforts have been mainly based on one-dimensional (1D) nanowires. For instance, as early as in 2005, a high rotation-speed micromotor prototype made of metal nanowires was applied to drive a dust particle into controllable circular motion [11]. More recently, an artificial nanomotor composed of two nickel-nanowire arms with a central gold-nanowire body has been demonstrated to propel twelve body lengths per second [12]. On the other hand, a multitude of manners have been developed to drive the nanowire-based motors via transferring external energy into mechanical motion, e.g., by chemical fuels [13,14], acoustic [15], magnetic [16,17], optic [18–20] and electric-induced external energy [21]. Among them, the electrically driven technique exhibits benefits that go further than being applicable for wide spectrum of nanowires, regardless of their metallic or non-metallic nature and also enabling simultaneous control of lateral alignment and synchronous rotation [22,23]. More importantly, by combining alternating and constant electric fields via four-electrode configuration, the targeted nanowires can be positioned at an arbitrary location in between the electrodes [24–26], as well as efficiently carrying out contactless conductivity measurements [27,28].

However, it is still a significant challenge to precisely control the nanowire-based micromotors, because the viscous force dominates the motion with nonnegligible Brownian

motion in the nanometer scale with a very low Reynolds number [29,30]. This reinforces the necessity of developing miniaturized components in the micrometer scale (>10 μm), which is required by, for instance, a microrobot with size of several hundred micrometers [31,32]. From this perspective, two-dimensional (2D) microplates can be regarded as ideal candidates in composing the miniaturized motors in micrometer scale. For example, Enachi et al. developed a micromembrane consisting of TiO_2 nanotube arrays, and the micromembrane with lateral size larger than 100 μm^2 demonstrated an effective cargo loading and transport under UV stimuli [33]. Another planar "pancake-like" micromachine with diameter of 300 μm has been recently reported, in which light-controlled heartbeat-like pumping function was realized [34]. It should be clarified that "2D" here not only refers to a nanosheet with thickness less than 10 nm, but also include other planar configurations, as long as the lateral size is much larger than the thickness. Aside from the abovementioned 2D micromotors controlled by light stimuli, a diversity of other manners has been applied to power 2D micromotors, such as fuel-driven and magnetically driven techniques [35–42]. Nevertheless, the experimental work relating to 2D micromotors still lags its 1D-nanowire counterpart mainly because of two aspects, i.e., suitable 2D material and optimal precisely controlled technique.

In this work, we have systematically studied high-speed rotating micromotors based on all-inorganic perovskite $CsPbBr_3$ microplates precisely controlled by external electric field, and further determined the electrical conductivity of $CsPbBr_3$ microplate in a contactless manner. Firstly, in terms of the 2D material, $CsPbBr_3$ microplates have been implemented in bewildering variety of different electrical and optoelectronic applications, owing to its large absorption coefficient, high photoluminescence quantum efficiency, ambipolar semiconductor characteristics, gradually improved environment stability [43–48]. Secondly, as for the external stimuli, inspired by the electric-driven nanowire micromotors and assisted by systematic physical simulations, we have applied the four-electrode configuration to precisely control the rotation speed of the 2D microplates, which reaches up to 16.4 × 2π rad/s. The electrical conductivity measured using this four-electrode system is approximately 10^{-9}–10^{-8} S/m. Our work has extended the investigations on AC electric field-controlled micromotors from 1D to 2D scale, offering opportunities to develop micromotors with new configuration.

2. Materials and Methods

2.1. Synthesis of $CsPbBr_3$ Microplates

Firstly, under the condition of stirring magnetically, we injected 0.2 mL precursor (1 mmol CsBr and 0.5 mmol $PbBr_2$ dissolved in 15 mL DMSO) into 1 mL octadecylamine/acetic acid solution (0.05 g/mL). This is followed by the addition of 15 mL toluene into the solution with further magnetic stirring. Next, the chemical reaction was stopped by centrifugation at a speed of 5000 rpm for one minute. The precipitation was eventually redispersed in toluene and washed once again, and then dispersed in 4 mL of toluene.

2.2. Device Characterization

The dynamic process of the $CsPbBr_3$ microplates suspended in solution were observed via a Seiwa Optical Microscope coupled with a CCD imaging acquisition device. The alternating electrical field was applied by a RIGOL DG1022U function generator, coupled with a Agitek ATA-2082 High Voltage Amplifier. Regarding the setup of the four-electrode system, a 1 mm thick copper plate was firstly cut into rectangular copper strips of 15 mm × 1 mm, then a glass plate of 30 mm × 20 mm was used as the carrier and four copper strips were placed on the glass plate in pairs with 1.5 mm in between, as schematically illustrated in Figure 1a. Afterwards, epoxy resin was poured around the copper strips. A circular area with a diameter of 10 mm was left in the middle. This process was completed by curing for 60 s at 120 °C via a hotplate.

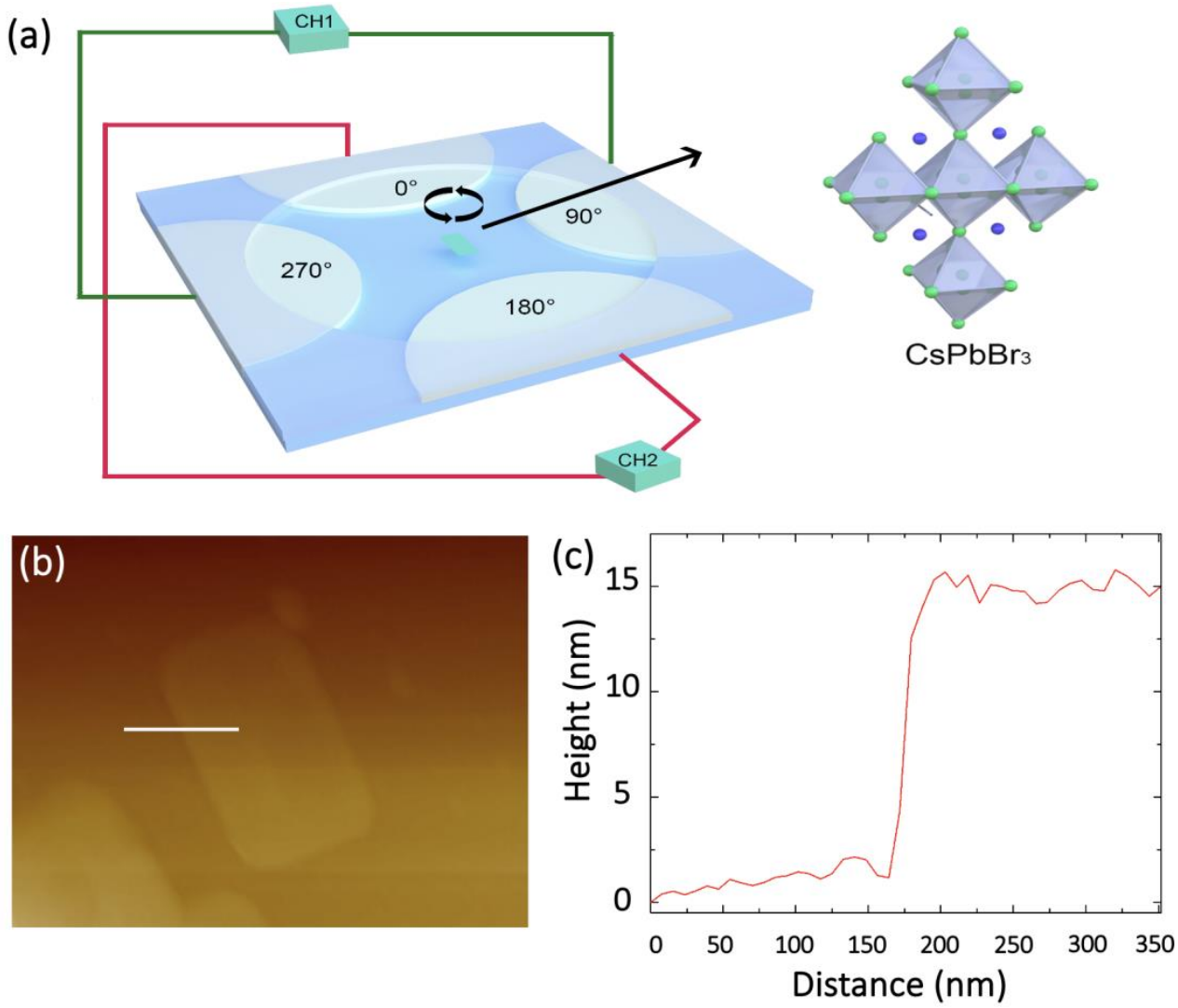

Figure 1. (**a**) Schematic illustration of the four-electrode configuration for biasing micromotor, with inset showing the crystalline structure of $CsPbBr_3$. (**b**) AFM image of a typical single $CsPbBr_3$ nanosheet. (**c**) Cross-sectional profile of the typical single $CsPbBr_3$ nanosheet marked by the straight white line in (**b**).

3. Results and Discussion

Figure 1a presents the schematic illustration of the four-electrode experimental configuration, with inset showing a portion of crystalline unit of $CsPbBr_3$, in which the copper electrodes are partially covered by epoxy resin, with a glass as the substrate. The $CsPbBr_3$ microplates dispersed in the solution of tetradecane are syringe-dropped in the center area surrounded by the four-metal electrodes. The dispersed single $CsPbBr_3$ microplate is a pile of multilayer nanosheets with consistent lattice orientation rather than randomly ordered thin nanosheets [49]. Figure 1b demonstrates a typical single layer of $CsPbBr_3$ nanosheet, from which the microplate can be constructed. It can be observed that the height of a typical $CsPbBr_3$ nanosheet is approximately 15 nm, as shown in the cross-sectional profile in Figure 1c.

Firstly, to determine the optimized electrode configuration, we have systematically simulated the electric field distribution in the center of the orthogonal four-electrode system, both on 2D- and 3D-scale with the help of COMSOL Multiphysics 5.4. The system consists of four electrodes, which are connected to the external AC circuit, as shown in Figure 1a. In our simulations, we only simulate the field distribution when the AC circuit is just turned on, i.e., when $t = 0$ as described later in Equation (1). On the 2D scale, we have simulated different electrode shapes to optimize its electrical stability for the contactless conductivity

measurements elaborated later in this work. The gradient of the electric field can greatly affect its stability. Therefore, a reasonable design of the electrode to reduce the gradient of the applied electric field without sacrificing the field strength is of great importance to the electrical characteristics of the microplates. Figure 2 compares the electric potential distribution of different electrode shapes, including round electrodes, square electrodes and concaved electrodes. It can be clearly observed that the round electrodes provide the optimized electric field distribution, i.e., a relatively strong and uniform electric field between the electrodes, as demonstrated in Figure 2a.

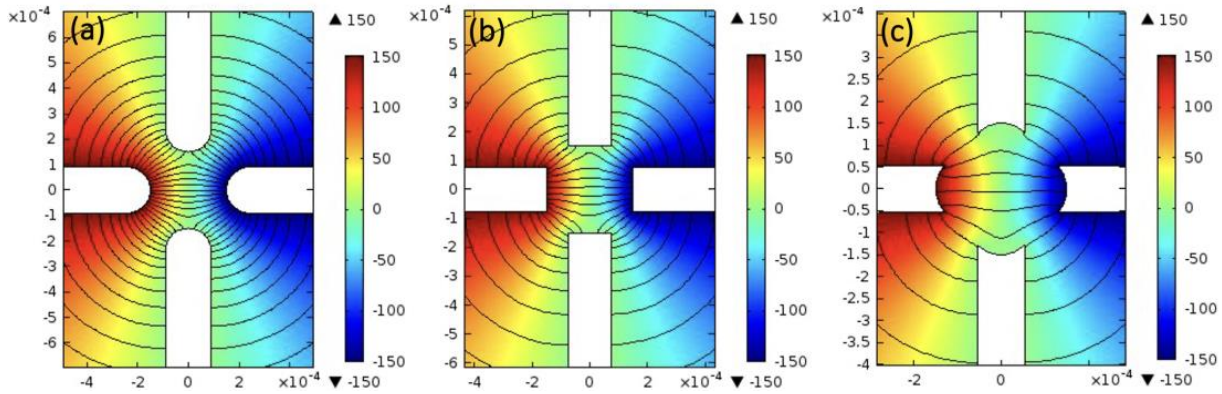

Figure 2. (**a**–**c**) Electric potential distribution of various electrode shapes, i.e., round electrodes, square electrodes and concaved electrodes. (length unit: m).

On the 3D scale, we have simulated and measured the electric field stability at different depths to obtain the most suitable observation depth area. Figure 3 provides the geometric model on the 3D scale, as well as the electric potential distribution. Through the simulation, we can conclude that the most suitable observation depth ranges from 50 µm to 180 µm using round-shape electrodes, which have been selected as the actual biasing configuration in our experiments.

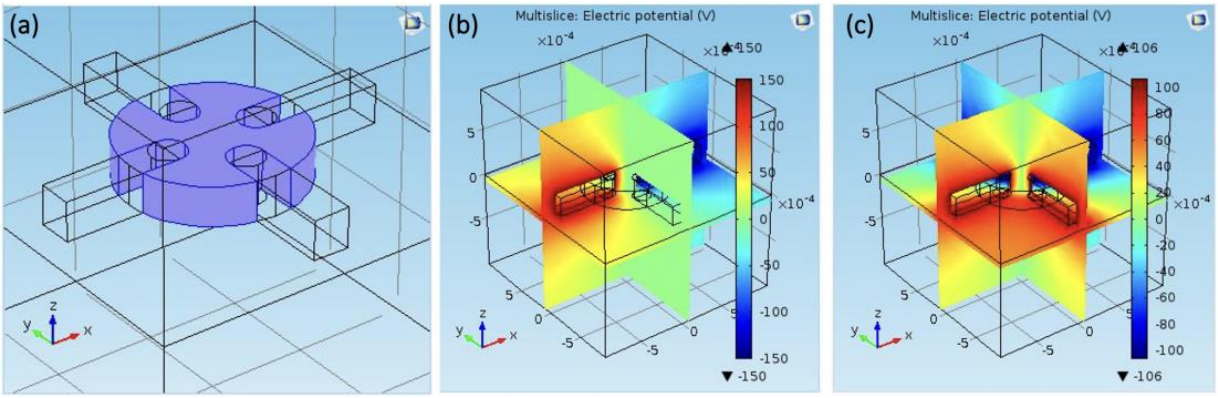

Figure 3. Electric potential distribution on 3D scale. (**a**) Geometry of the simulation electrodes. (**b**,**c**) Electrical potential distribution for two different voltage configurations with voltage applied across different electrodes (length unit: m).

Regarding the operating mechanism, a rotating electric field can be generated by applying alternating-current (AC) voltage to the two sets of orthogonal metal electrodes with a $\pi/2$ phase difference, i.e.,

$$\begin{aligned} U_1 &= U_0 \cos \omega t \\ U_2 &= U_0 \cos(\omega t - \tfrac{\pi}{2}) \end{aligned} \quad (1)$$

where U_0 is the amplitude and ω is the angular velocity. The electric field near the center exhibits a constant amplitude and rotates at the same angular velocity ω. The amplitude of the electric field E_0 is related to U_0 according to Equation (2) as follows:

$$E_0 = \alpha \frac{U_0}{d} \tag{2}$$

where d is the spacing between electrode and α is a correction factor, which is typically less than 1. This rotating electric field can exert a torque T on the microplates governed by the following equation [50]:

$$T = -V\varepsilon_2 E_0^2 [\frac{(1-\tau_1/\tau_2)\omega\tau_1}{1+(\omega\tau_1)^2}] \tag{3}$$

Here, V is the volume of the microplate. $\tau_1 = \varepsilon_1/\sigma_1$ and $\tau_2 = \varepsilon_2/\sigma_2$ are the characteristic relaxation times of the fluid and the microplate, respectively. ε_i and σ_i (i = 1, 2) represent the corresponding electric permittivity and conductivity, respectively. In this study, the fluid possesses a very low conductivity, i.e., $\sigma_1 << \sigma_2$ and its relaxation time is much larger than that of the microplate, i.e., $\tau_1 >> \tau_2$. Based on this relation, Equation (3) can be simplified as:

$$T = -V\varepsilon_2 E_0^2 \frac{(\omega\tau_1)^2}{1+(\omega\tau_1)^2}(\frac{1}{\omega\tau_1} - \frac{1}{\omega\tau_2}) \approx VE_0^2\frac{\sigma_2}{\omega} \tag{4}$$

As indicated by Equation (4), the torque T is linearly proportional to the conductivity of the microplate. In the limit of low Reynolds number, the microplate suspended in the fluid can rotate at a constant velocity Ω in response to the torque:

$$\gamma\Omega = T \tag{5}$$

where γ represents the rotational drag coefficient depending on the particle size and shape. For the microplate with much larger lateral size compared with its thickness, γ can be determined as [51,52]:

$$\gamma = \frac{8\eta}{m\pi}V \tag{6}$$

where η is the viscosity of the fluid and m is the ratio of the thickness and lateral size of the microplate. Combining Equations (4)–(6), we can eventually obtain a relation governing the rotating velocity of the microplate, as presented in Equation (7) as follows:

$$\Omega = \frac{m\pi}{8\eta\omega}\sigma_2 E_0^2 \tag{7}$$

Figure 4 demonstrates dynamic process of a rotating $CsPbBr_3$ microplate driven by AC frequency of approximately 1.5 kHz. By applying AC voltages with different phase and frequencies in the range of 10 Hz to 100 kHz on the quadruple electrodes, a rotating AC electric field can be created to drive the $CsPbBr_3$ microplate, as shown in Video S1 and Video S2 of Supplementary Materials. When a rotating AC electric field is applied to the four-electrode system, an electrical torque is imposed on the induced dipole moment of the $CsPbBr_3$ microplates and force it to rotate. The rotation speed of the $CsPbBr_3$ microplates can be precisely manipulated by adjusting the frequency of the AC electric field.

Due to influencing factors such as dielectric strain and electrolyte shielding effect, to minimize contact with the substrate to reduce the deviation in characterizing 2D material becomes increasingly important. Herein, we have obtained the specific conductivity of the $CsPbBr_3$ microplates in a contactless manner. By processing the rotation of $CsPbBr_3$ microplates through image processing, we can obtain the rotation speed of the $CsPbBr_3$ microplates based on previously derived Equation (7). The conductivity of the $CsPbBr_3$ microplates measured by this contactless manner ranges from 10^{-9}–10^{-8} S/m. Moreover, as shown in Figure 5, the rotation speed of the $CsPbBr_3$ microplates decreases with increasing the frequency of the AC electric field. The aforementioned theoretical derivation

can be used not only for contactless measurement, but also for precise manipulation of microplates under an external AC electric field. This manipulation principle provides a feasible way to precisely control the rotation of 2D micromotors.

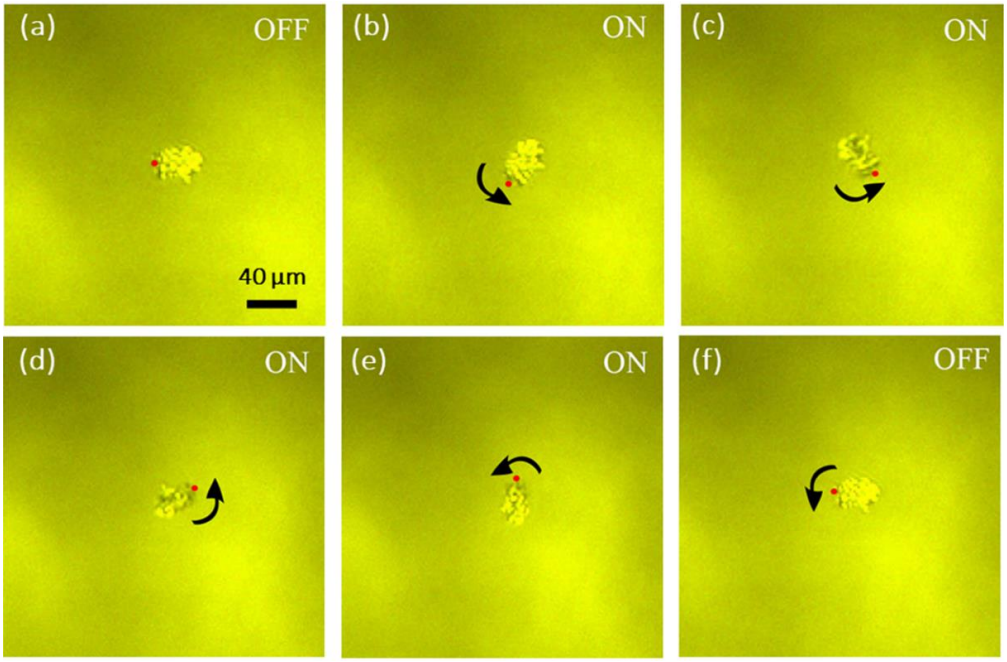

Figure 4. (**a**–**f**) Snap shots of rotating $CsPbBr_3$ microplates in every 1/6 s.

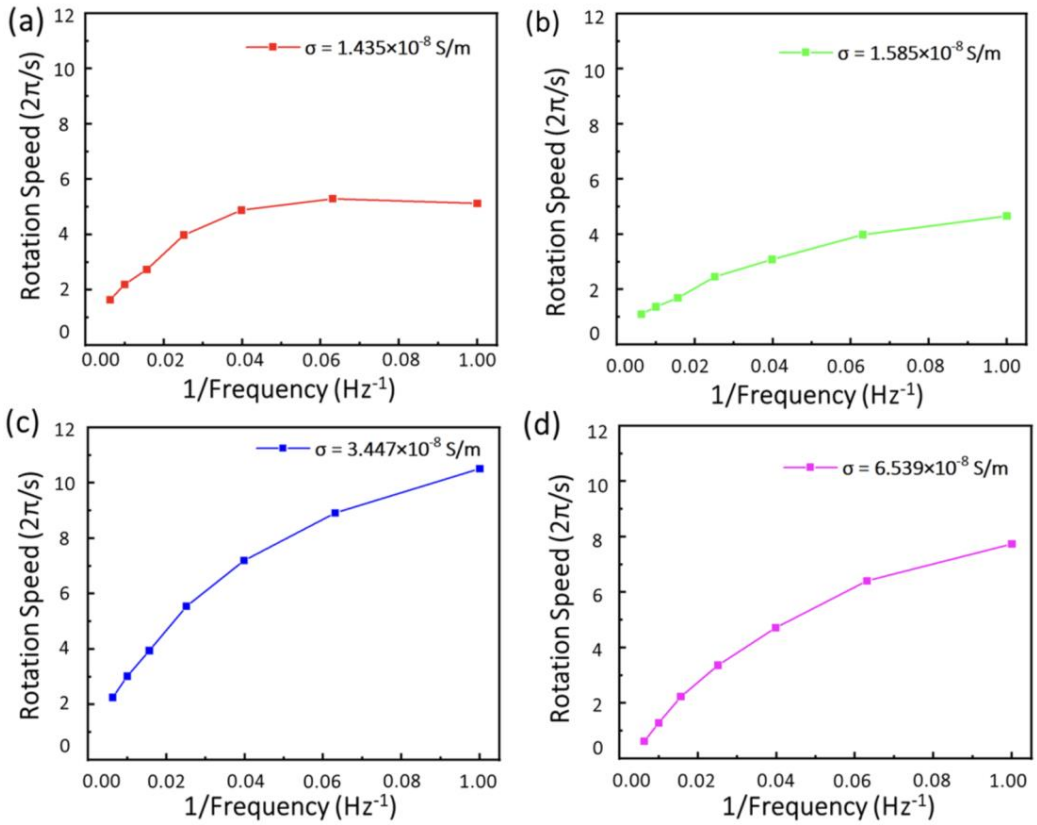

Figure 5. (**a**–**d**) Rotation speed dependent on AC frequency of the $CsPbBr_3$ microplates with different sizes in the range from 690 μm^2, 720 μm^2, 1040 μm^2 to 1470 μm^2.

4. Conclusions

In summary, we applied AC electric field to precisely control all-inorganic perovskite $CsPbBr_3$ microplates to rotate with high speed and further determined the electrical conductivity in a contactless manner. Moreover, the specific movement mechanism of the 2D material was systematically analyzed. In addition, the 2D and 3D simulation can confirm that the round electrode exhibits the optimized stability. Our work extended the investigations on AC electric field-controlled micromotors from 1D to 2D scale, shedding new light on developing micromotors with new configuration.

Supplementary Materials: The following are available online at https://www.mdpi.com/article/10.3390/mi12101228/s1, Video S1: Dynamic rotation of a typical $CsPbBr_3$ microplate at low AC frequency. Video S2: Dynamic rotation of a typical $CsPbBr_3$ microplate at high frequency.

Author Contributions: Conceptualization, Y.G. and X.L.; methodology, R.Z. and D.H.; software, R.Z., D.H. and S.G.; original draft preparation, R.Z.; writing—review and editing, Z.R. and X.L.; visualization, X.L.; supervision, Y.G. and X.L.; project administration, Y.G. and X.L.; funding acquisition, Y.G. and X.L. All authors have read and agreed to the published version of the manuscript.

Funding: This research was funded by the Natural Science Foundation of Shandong Province, China, grant number ZR2020QF104, the National Key R&D Program of China (No. 2017YFA0305500), the Natural Science Foundation of Jiangsu Province (No. BK20200071) and the Fundamental Research Funds for the Central Universities (No. 30919011298).

Conflicts of Interest: The authors declare no conflict of interest.

References

1. Tu, Y.F.; Peng, F.; Wilson, D.A. Motion manipulation of micro- and nanomotors. *Adv. Mater.* **2017**, *29*, 1701970. [CrossRef] [PubMed]
2. Xu, B.; Zhang, B.; Wang, L.; Huang, G.; Mei, Y. Tubular micro/nanomachines: From the basics to recent advances. *Adv. Funct. Mater.* **2018**, *28*, 1705872. [CrossRef]
3. Sipova-Jungova, H.; Andren, D.; Jones, S.; Kall, M. Nanoscale inorganic motors driven by light: Principles, realizations, and opportunities. *Chem. Rev.* **2020**, *120*, 269–287. [CrossRef] [PubMed]
4. De Ávila, B.E.F.; Angsantikul, P.; Li, J.; Lopez-Ramirez, M.A.; Ramirez-Herrera, D.E.; Thamphiwatana, S.; Chen, C.; Delezuk, J.; Samakapiruk, R.; Ramez, V.; et al. Micromotor-enabled active drug delivery for in vivo treatment of stomach infection. *Nat. Commun.* **2017**, *8*, 272. [CrossRef]
5. De Avila, B.E.F.; Angsantikul, P.; Li, J.; Gao, W.; Zhang, L.; Wang, J. Micromotors go in vivo: From test tubes to live animals. *Adv. Funct. Mater.* **2018**, *28*, 1705640. [CrossRef]
6. Jurado-Sanchez, B.; Wang, J. Micromotors for environmental applications: A review. *Environ. Sci. Nano* **2018**, *5*, 1530–1544. [CrossRef]
7. Dong, R.F.; Cai, Y.P.; Yang, Y.R.; Gao, W.; Ren, B.Y. Photocatalytic micro/nanomotors: From construction to applications. *Acc. Chem. Res.* **2018**, *51*, 1940–1947. [CrossRef] [PubMed]
8. Guix, M.; Mayorga-Martinez, C.C.; Merkoci, A. Nano/micromotors in (bio) chemical science applications. *Chem. Rev.* **2014**, *114*, 6285–6322. [CrossRef] [PubMed]
9. Li, Y.; Liu, X.; Xu, X.; Xin, H.; Zhang, Y.; Li, B. Red-blood-cell waveguide as a living biosensor and micromotor. *Adv. Funct. Mater.* **2019**, *29*, 1905568. [CrossRef]
10. Zhang, X.; Chen, C.; Wu, J.; Ju, H. Bubble-propelled jellyfish-like micromotors for DNA sensing. *ACS Appl. Mater. Interfaces* **2019**, *11*, 13581–13588. [CrossRef] [PubMed]
11. Fan, D.L.; Zhu, F.Q.; Cammarata, R.C.; Chien, C.L. Controllable high-speed rotation of nanowires. *Phys. Rev. Lett.* **2005**, *94*, 247208. [CrossRef]
12. Li, T.; Li, J.; Morozov, K.I.; Wu, Z.; Xu, T.; Rozen, I.; Leshansky, A.M.; Li, L.; Wang, J. Highly efficient freestyle magnetic nanoswimmer. *Nano Lett.* **2017**, *17*, 5092–5098. [CrossRef] [PubMed]
13. Sanchez, S.; Soler, L.; Katuri, J. Chemically powered micro- and nanomotors. *Angew. Chem. Int. Edit.* **2015**, *54*, 1414–1444. [CrossRef] [PubMed]
14. Sahore, V.; Kreidermacher, A.; Khan, F.Z.; Fritsch, I. Visualization and measurement of natural convection from electrochemically-generated density gradients at concentric microdisk and ring electrodes in a microfluidic system. *J. Electrochem. Soc.* **2016**, *163*, H3135–H3144. [CrossRef]
15. Ahmed, S.; Wang, W.; Bai, L.; Gentekos, D.T.; Hoyos, M.; Mallouk, T.E. Density and shape effects in the acoustic propulsion of bimetallic nanorod motors. *ACS Nano* **2016**, *10*, 4763–4769. [CrossRef]

16. Cao, Q.L.; Fan, Q.; Chen, Q.; Liu, C.T.; Han, X.T.; Li, L. Recent advances in manipulation of micro- and nano-objects with magnetic fields at small scales. *Mater. Horiz.* **2020**, *7*, 638–666. [CrossRef]
17. Gu, Y.; Kornev, K.G. Ferromagnetic nanorods in applications to control of the in-plane anisotropy of composite films and for in situ characterization of the film rheology. *Adv. Funct. Mater.* **2016**, *26*, 3796–3808. [CrossRef]
18. Villa, K.; Pumera, M. Fuel-free light-driven micro/nanomachines: Artificial active matter mimicking nature. *Chem. Soc. Rev.* **2019**, *48*, 4966–4978. [CrossRef] [PubMed]
19. Cao, F.; Yu, D.; Gu, Y.; Chen, J.; Zeng, H. Novel optoelectronic rotors based on orthorhombic CsPb (Br/I) 3 nanorods. *Nanoscale* **2019**, *11*, 3117–3122. [CrossRef] [PubMed]
20. Chen, H. Controllable fast and slow light in photonic-molecule optomechanics with phonon pump. *Micromachines* **2021**, *12*, 1074. [CrossRef] [PubMed]
21. Roche, J.; Carrara, S.; Sanchez, J.; Lannelongue, J.; Loget, G.; Bouffier, L.; Fischer, P.; Kuhn, A. Wireless powering of e-swimmers. *Sci. Rep.* **2014**, *4*, 6705. [CrossRef] [PubMed]
22. Farain, K.; Esfandiar, A.; Moshfegh, A.Z. Universal rotation of nanowires in static uniform electric fields in viscous dielectric liquids. *Appl. Phys. Lett.* **2018**, *113*, 063101. [CrossRef]
23. Farain, K.; Esfandiar, A.; Moshfegh, A.Z. Shooting at the nanoscale: Collection and acceleration of nanowires with an external electric field. *Appl. Phys. Lett.* **2019**, *114*, 013102. [CrossRef]
24. Fan, D.; Yin, Z.; Cheong, R.; Zhu, F.Q.; Cammarata, R.C.; Chien, C.L.; Levchenko, A. Subcellular-resolution delivery of a cytokine through precisely manipulated nanowires. *Nat. Nanotechnol.* **2010**, *5*, 545–551. [CrossRef]
25. Liang, Z.; Fan, D. Visible light-gated reconfigurable rotary actuation of electric nanomotors. *Sci. Adv.* **2018**, *4*, eaau0981. [CrossRef] [PubMed]
26. Liang, Z.X.; Teal, D.; Fan, D.L. Light programmable micro/nanomotors with optically tunable in-phase electric polarization. *Nat. Commun.* **2019**, *10*, 5275. [CrossRef] [PubMed]
27. Akin, C.; Yi, J.; Feldman, L.C.; Durand, C.; Hus, S.M.; Li, A.-P.; Filler, M.A.; Shan, J.W. Contactless determination of electrical conductivity of one-dimensional nanomaterials by solution-based electro-orientation spectroscopy. *ACS Nano* **2015**, *9*, 5405–5412. [CrossRef] [PubMed]
28. Yuan, W.; Tutuncuoglu, G.; Mohabir, A.; Liu, L.; Feldman, L.C.; Filler, M.A.; Shan, J.W. Contactless electrical and structural characterization of semiconductor nanowires with axially modulated doping profiles. *Small* **2019**, *15*, 1805140. [CrossRef] [PubMed]
29. Li, L.Q.; Wang, J.Y.; Li, T.L.; Song, W.P.; Zhang, G.Y. A unified model of drag force for bubble-propelled catalytic micro/nano-motors with different geometries in low reynolds number flows. *J. Appl. Phys.* **2015**, *117*, 104308. [CrossRef]
30. Novotny, F.; Wang, H.; Pumera, M. Nanorobots: Machines squeezed between molecular motors and micromotors. *Chem* **2020**, *6*, 867–884. [CrossRef]
31. Beladi-Mousavi, S.M.; Khezri, B.; Matejkova, S.; Sofer, Z.; Pumera, M. Supercapacitors in motion: Autonomous microswimmers for natural-resource recovery. *Angew. Chem. Int. Ed.* **2019**, *58*, 13340–13344. [CrossRef] [PubMed]
32. Kummer, M.P.; Abbott, J.J.; Kratochvil, B.E.; Borer, R.; Sengul, A.; Nelson, B.J. Octomag: An electromagnetic system for 5-dof wireless micromanipulation. *IEEE Trans. Robot.* **2010**, *26*, 1006–1017. [CrossRef]
33. Enachi, M.; Guix, M.; Postolache, V.; Ciobanu, V.; Fomin, V.M.; Schmidt, O.G.; Tiginyanu, I. Light-induced motion of microengines based on microarrays of TiO_2 nanotubes. *Small* **2016**, *12*, 5497–5505. [CrossRef] [PubMed]
34. Li, M.; Su, Y.; Zhang, H.; Dong, B. Light-powered direction-controlled micropump. *Nano Res.* **2018**, *11*, 1810–1821. [CrossRef]
35. Gai, M.; Frueh, J.; Hu, N.; Si, T.; Sukhorukov, G.B.; He, Q. Self-propelled two dimensional polymer multilayer plate micromotors. *Phys. Chem. Chem. Phys.* **2016**, *18*, 3397–3401. [CrossRef] [PubMed]
36. Hu, N.; Zhang, B.; Gai, M.; Zheng, C.; Frueh, J.; He, Q. Forecastable and guidable bubble-propelled microplate motors for cell transport. *Macromol. Rapid Commun.* **2017**, *38*, 1600795. [CrossRef] [PubMed]
37. Cohen, K.J.; Rubinstein, B.Y.; Kenneth, O.; Leshansky, A.M. Unidirectional propulsion of planar magnetic nanomachines. *Phys. Rev. Appl.* **2019**, *12*, 014025. [CrossRef]
38. Chen, M.F.; Shinde, A.; Wang, L.; Ye, C.; Zeng, M.X.; Yan, Q.; Lin, P.C.; Chen, Y.; Cheng, Z.D. Rainbows in a vial: Controlled assembly of 2D colloids in two perpendicular external fields. *2D Mater.* **2019**, *6*, 025031. [CrossRef]
39. Piazza, R. Thermophoresis: Moving particles with thermal gradients. *Soft Matter* **2008**, *4*, 1740–1744. [CrossRef]
40. Shinde, A.; Huang, D.L.; Saldivar, M.; Xu, H.F.; Zeng, M.X.; Okeibunor, U.; Wang, L.; Mejia, C.; Tin, P.; George, S.; et al. Growth of colloidal nanoplate liquid crystals using temperature gradients. *ACS Nano* **2019**, *13*, 12461–12469. [CrossRef] [PubMed]
41. Son, C.H.; Ji, B.Q.; Park, J.Y.; Feng, J.; Kim, S. A magnetically actuated superhydrophobic ratchet surface for droplet manipulation. *Micromachines* **2021**, *12*, 325. [CrossRef] [PubMed]
42. Zeng, M.X.; Huang, D.L.; Wang, P.M.; King, D.; Peng, B.L.; Luo, J.H.; Lei, Q.; Zhang, L.C.; Wang, L.; Shinde, A.; et al. Autonomous catalytic nanomotors based on 2D magnetic nanoplates. *ACS Appl. Nano Mater.* **2019**, *2*, 1267–1273. [CrossRef]
43. Huo, C.; Liu, X.; Wang, Z.; Song, X.; Zeng, H. High-Performance low-voltage-driven phototransistors through CsPbBr3–2D crystal van der Waals heterojunctions. *Adv. Opt. Mater.* **2018**, *6*, 1800152. [CrossRef]
44. Liu, X.; Yu, D.; Huo, C.; Song, X.; Gao, Y.; Zhang, S.; Zeng, H. A perovskite light-emitting device driven by low-frequency alternating current voltage. *Adv. Opt. Mater.* **2018**, *6*, 1800206. [CrossRef]

45. Liu, X.; Yu, D.; Song, X.; Zeng, H. Metal halide perovskites: Synthesis, ion migration, and application in field-effect transistors. *Small* **2018**, *14*, 1801460. [CrossRef] [PubMed]
46. Gu, Z.K.; Zhou, Z.H.; Huang, Z.D.; Wang, K.; Cai, Z.R.; Hu, X.T.; Li, L.H.; Li, M.Z.; Zhao, Y.S.; Song, Y.L. Controllable growth of high-quality inorganic perovskite microplate arrays for functional optoelectronics. *Adv. Mater.* **2020**, *32*, 1908006. [CrossRef] [PubMed]
47. Liu, X.; Tan, X.; Liu, Z.; Ye, H.; Sun, B.; Shi, T.; Tang, Z.; Liao, G. Boosting the efficiency of carbon-based planar CsPbBr3 perovskite solar cells by a modified multistep spin-coating technique and interface engineering. *Nano Energy* **2019**, *56*, 184–195. [CrossRef]
48. Wang, H.; Zhang, X.; Wu, Q.; Cao, F.; Yang, D.; Shang, Y.; Ning, Z.; Zhang, W.; Zheng, W.; Yan, Y.; et al. Trifluoroacetate induced small-grained CsPbBr3 perovskite films result in efficient and stable light-emitting devices. *Nat. Commun.* **2019**, *10*, 665. [CrossRef] [PubMed]
49. Liu, X.; Yu, D.; Cao, F.; Li, X.; Ji, J.; Chen, J.; Song, X.; Zeng, H. Low-voltage photodetectors with high responsivity based on solution-processed micrometer-scale all-inorganic perovskite nanoplatelets. *Small* **2017**, *13*, 1700364. [CrossRef]
50. Jones, T.B. *Electromechanics of Particles*; Cambridge University Press: Cambridge, UK, 2005.
51. Dusenbery, D.B. *Living at Micro Scale: The Unexpected Physics of Being Small*; Harvard University Press: Cambridge, UK, 2009.
52. Gu, Y.; Zeng, H. Optically tunable quincke rotation of a nanometer-thin oblate spheroid. *Phys. Rev. Fluids* **2017**, *2*, 083701. [CrossRef]